

Feature Alignment with Equivariant Convolutions for Burst Image Super-Resolution

Xinyi Liu
Xi'an Jiaotong University
xinyi12525@gmail.com

Feiyu Tan
Xi'an Jiaotong University
tanfy929@stu.xjtu.edu.cn

Qi Xie
Xi'an Jiaotong University
xie.qi@xjtu.edu.cn

Qian Zhao*
Xi'an Jiaotong University
timmy.zhaoqian@xjtu.edu.cn

Deyu Meng
Xi'an Jiaotong University
dymeng@xjtu.edu.cn

Abstract

Burst image processing (BIP), which captures and integrates multiple frames into a single high-quality image, is widely used in consumer cameras. As a typical BIP task, Burst Image Super-Resolution (BISR) has achieved notable progress through deep learning in recent years. Existing BISR methods typically involve three key stages: alignment, upsampling, and fusion, often in varying orders and implementations. Among these stages, alignment is particularly critical for ensuring accurate feature matching and further reconstruction. However, existing methods often rely on techniques such as deformable convolutions and optical flow to realize alignment, which either focus only on local transformations or lack theoretical grounding, thereby limiting their performance. To alleviate these issues, we propose a novel framework for BISR, featuring an equivariant convolution-based alignment, ensuring consistent transformations between the image and feature domains. This enables the alignment transformation to be learned via explicit supervision in the image domain and easily applied in the feature domain in a theoretically sound way, effectively improving alignment accuracy. Additionally, we design an effective reconstruction module with advanced deep architectures for upsampling and fusion to obtain the final BISR result. Extensive experiments on BISR benchmarks show the superior performance of our approach in both quantitative metrics and visual quality.

1. Introduction

Image super-resolution is an important task in image processing. Conventionally, it is mainly dealt with in the context of Single Image Super Resolution (SISR) [10, 32] and significant progress has been made in the last decades. In

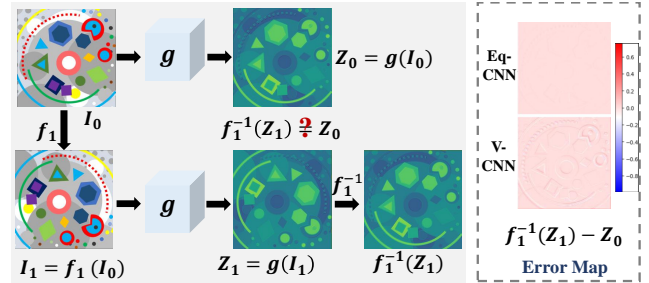


Figure 1. Illustration of transformation consistency in vanilla (V-CNN) and equivariant (Eq-CNN) convolutional networks. f_1 denotes a transformation (rotation in this example) and g is a CNN that extracts features from images. Suppose I_1 is the image obtained by applying f_1 to I_0 , i.e., $I_1 = f_1(I_0)$, and Z_0 and Z_1 are features extracted from I_0 and I_1 , respectively. We expect that Z_1 can be close to $f_1(Z_0)$, the transformation of Z_0 , such that one can align Z_1 to Z_0 in the feature domain by applying the inverse transformation f_1^{-1} , which can be learned by explicit supervision in the image domain. The right box compares the error between $f_1^{-1}(Z_1)$ and Z_0 , and it can be observed that Eq-CNN can more effectively achieve this goal than V-CNN.

recent years, by the advances in image acquisition technologies, a new kind of super-resolution technique, Burst Image Super-Resolution (BISR) [1, 4] has emerged as an increasingly valuable alternative. Unlike SISR, BISR reconstructs a high-resolution (HR) image by leveraging a sequence of low-resolution (LR) images captured in rapid succession, making it inherently more robust to noise and artifacts. Despite its advantages, BISR faces significant challenges, including accurate alignment for handling motion variations and effective multi-frame fusion.

The general pipeline for BISR typically involves three key stages: alignment, upsampling, and fusion, with their order and implementation varying across methods. Among them, alignment generally plays a crucial role in addressing spatial misalignments between successive frames. It

ensures accurate feature matching and enables high-quality image reconstruction. Currently, existing methods mainly adopt two kinds of approaches to realize alignment, i.e., Deformable Convolution Networks (DCN) [8] and optical flow [18]. For instance, in [11, 12], DCN was used to extract and align features, demonstrating strong capabilities in modeling local spatial transformations, and in [20], optical flow was adopted, enabling supervised alignment in the image domain. However, although they have demonstrated their effectiveness in BISR, these two approaches still have limitations. Specifically, DCN may not well model the global transformation [20] and is also difficult to be explicitly supervised using the image domain information, while the optical flow estimated in the image domain may not be strictly valid in the feature domain.

To alleviate these limitations of alignment in existing methods, we propose to leverage equivariant convolutional networks (Eq-CNNs) [14, 34, 36] with learnable transformation matrices as a solution. Compared with vanilla convolutional networks (V-CNNs) [21, 23], Eq-CNNs can extract features that are theoretically equivariant to input images under certain spatial transformations, e.g., rotation and translation. Then, suppose each source frame within burst images can be approximately modeled by such a transformation (or more specifically, rotation plus translation) of the reference frame due to the acquisition mechanism [1]. In that case, the equivariance property of Eq-CNNs enables us to learn the transformation (or its inverse) with the image domain supervision and then apply the inverse transformation in the feature domain to achieve an easy while theoretically sound alignment, as illustrated in Fig. 1.

With the aligned features as aforementioned, we further designed a reconstruction module for upsampling and fusion to generate the final sRGB image using advanced techniques. Specifically, considering its ability in capturing intricate inter-frame correlations, we adopt the Multi-Dconv Head Transposed Attention (MDTA) block [37] for feature interaction among frames; and due to its flexibility in multi-scale upsampling, we use the implicit neural representation (INR) technique [22] to upsample the features for final fusion, following [20].

To summarize, our contributions are as follows:

- We propose a new alignment framework for BISR based on Eq-CNN, which enables us to learn the alignment transformation with image domain supervision and apply it in the feature domain in a theoretically sound way. The corresponding theoretical analysis also advances the theory of Eq-CNN to a certain extent.
- We incorporate the proposed alignment framework with advanced techniques for upsampling and fusion, including MDTA from Restormer and INR, and build a new deep model for the BISR task.
- We apply the proposed model to BISR benchmarks,

demonstrate its superiority against current state-of-the-art methods.

2. Related Work

2.1. Burst image super-resolution

BISR and its related task, Muti Frame Super-Resolution (MFSR), have been extensively studied using both traditional approaches and deep learning techniques. The pioneering work by Tsai et al. [28] tackled the problem in the frequency domain, while subsequent research [13, 19, 29] put more focus on the spatial domain for resolution enhancement.

With the rapid advances of deep learning, significant progress has been made in this area. Initial studies [26, 30] employed relatively simple network architectures to address the MFSR task. Then, Bhat et al. [2] proposed a BISR pipeline incorporating alignment, feature fusion, and upsampling modules, which has inspired numerous studies [3, 9, 11, 12, 24, 25, 27]. The first real-world burst SR benchmark was also introduced in [2].

Within the BISR pipeline, alignment plays an important role and was specifically emphasized by Kang et al. [20]. While many methods adopted DCN [8] for alignment [11, 12], it is not effective enough to cover global alignments, as pointed in [20]. In contrast, Kang et al. [20] introduced optical flow [18] to achieve alignment, improving performance. However, since the optical flow is estimated in the image domain, there is no strict guarantee that the alignment transformation is theoretically valid in the feature domain. This motivates us to develop a more theoretically sound alignment technique via Eq-CNN.

In addition to alignment, the upsampling and fusion stages have also been advanced by recently developed neural architectures and techniques. For example, Transformer-based architectures [31] were adopted in the Burstormer [12] and GMTNet [25] methods to enhance feature representation by long-range dependency modeling; MAMBA [15] was introduced in QMambaBSR [9] to better integrate subpixel information through efficient state-space modeling; diffusion models [16] was employed in BSRD [27] to refine reconstruction results; and INR [6, 22] technique was used in BurstM [20] to realize multi-scale upsampling.

2.2. Equivariant convolutions

One of the key reasons for the success of CNNs in computer vision tasks is their inherent translation-equivariance, which ensures spatial consistency by making a translation in the input equivalent to translations in all intermediate feature maps and the output. Based on this concept, rotation-equivariant convolutions have been further developed. For instance, GCNN [7] and HexaConv [17] explicitly incorporate $\frac{\pi}{2}$ and $\frac{\pi}{3}$ rotational equivariance, respectively. More-

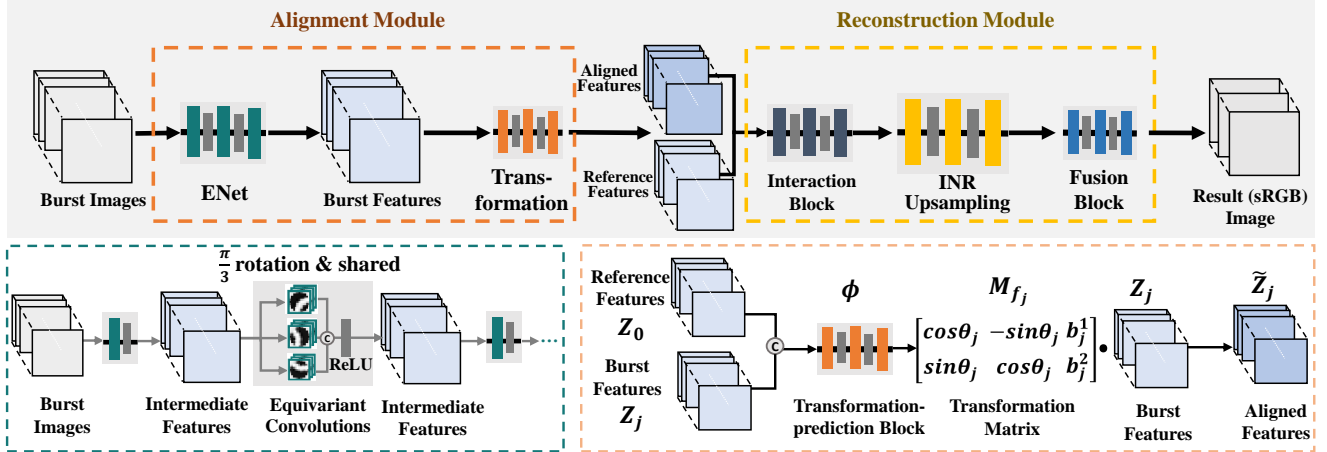


Figure 2. Overview of our proposed method. The top row shows the whole workflow. The bottom left shows the detailed equivariant convolution layers of ENet. The bottom right shows the process of feature alignment by predicted transformation, as in Section 3.2.2.

over, Xie et al. [35] proposed a Fourier series expansion-based filter parameterization, extending rotation equivariance to nearly continuous degrees, which has demonstrated its advanced capabilities and practical value in applications such as [14]. The equivariance property of Eq-CNNs provides a possibility for supervised learning of a transformation using the image domain information, which is still theoretically valid in the feature domain. This is crucial in the designing of our alignment framework, as discussed with more details in Section 3.1.

3. Proposed Method

We first provide preliminaries of equivariant convolutions to motivate our alignment framework for BISR. Then, we discuss the details of our proposed method, including the network architectures of both the alignment and reconstruction modules. We also provide a theoretical justification for the validity of the proposed alignment framework.

3.1. Motivation

We first briefly introduce the concept of equivariance in deep learning. Suppose g is a deep feature extractor mapping from input to the feature space and F is a transformation group, we say g is equivariant with respect to F if for any $f \in F$, it holds that $f(g(I)) = g(f(I))$, or equivalently, $g(I) = f^{-1}(g(f(I)))$ if f is invertible. Note that here, we abuse the notation f a little to denote the same transformation applied in different domains. It is well known that V-CNNs are only equivariant with respect to translation, while previous studies on equivariance [34, 35] constructed CNNs that are also equivariant with respect to rotation and reflection, which are often referred to as equivariant CNNs (Eq-CNNs).

The equivariance property of Eq-CNNs enables us to develop an effective and theoretically sound approach for

alignment. Specifically, we notice that burst images are captured by repeated exposures in a short time, and thus, the misalignments between frames are mainly caused by slight camera shifts and are generally not very spatially significant. Therefore, we may approximately model each source frame as a rotation and translation of the reference frame [1]. Then, if we use an Eq-CNN to extract features of the original frames, the transformation consistency between the image domain and feature domain can be naturally guaranteed. Consequently, we can learn such transformations (or their inverses) via the image domain supervision while applying them in the feature domain for alignment. The details are provided in Section 3.2.2.

3.2. Our method

3.2.1. Problem setting and processing pipeline

Given B low-resolution (LR) RAW burst frames $\{I_j^L\}_{j=0}^{B-1}$ with each $I_j^L \in \mathbb{R}^{h \times w \times 1}$, we first process it a 4-channel format following the RGGGB Bayer pattern [12, 20]. Then, one frame is selected as the reference frame, which serves as the reference for high-resolution (HR) reconstruction, and the rest frames are used to assist the reference one in super-resolving. The reconstructed HR image $I^S \in \mathbb{R}^{sh \times sw \times 3}$ is in sRGB format, where s is the scale factor. As shown in Fig. 2, our processing pipeline includes two main steps, i.e., alignment and reconstruction. The alignment step aims to extract and align features from the LR burst images using the Eq-CNN, and the reconstruction step tries to upsample and fuse the features to get the final reconstruction.

3.2.2. Alignment Module

Let I_0^L denote the RAW LR reference frame and $\{I_j^L\}_{j=1}^{B-1}$ represent the remaining source frames in the burst image. Following the discussions in Section 3.1, we approximately

model the relationship between each I_j^L ($j \neq 0$) and I_0^L as

$$I_j^L = f_j(I_0^L), \quad (1)$$

where f_j is a rotation-translation transformation. After feature extraction using an Eq-CNN g , which is referred to as *ENet* in Fig. 2, we can obtain features $Z_0 = g(I_0^L)$ and $Z_j = g(I_j^L)$, respectively. Assuming the equivariance property of g strictly holds, we have that

$$Z_j = g(I_j^L) = g(f_j(I_0^L)) = f_j(g(I_0^L)) = f_j(Z_0). \quad (2)$$

This indicates that, if we can accurately estimate f_j or f_j^{-1} in the image domain, the equivariance property of Eq-CNN allows us to directly apply f_j^{-1} to Z_j :

$$\tilde{Z}_j = f_j^{-1}(Z_j), \quad (3)$$

such that \tilde{Z}_j is well aligned to Z_0 .

Therefore, we learn f_j^{-1} via the image domain supervision with the following loss:

$$\mathcal{L}_{\text{align}} = \frac{1}{B-1} \sum_{j=1}^{B-1} \|f_j^{-1}(I_j^L) - I_0^L\|_2^2. \quad (4)$$

In practice, however, due to the discretization of the rotation angles in Eq-CNNs, we cannot strictly guarantee that $f_j^{-1}(Z_j) = Z_0$. Nevertheless, we can provide a theoretical justification to ensure that $f_j^{-1}(Z_j)$ can be close to Z_0 by minimizing Eq. (4). To ensure the smooth flow of the text, we put the theoretical results in Theorem 1 and Corollary 1 of Section 3.3 and continue to discuss our method here.

The next question is then how to parameterize the transformation f_j^{-1} . Since we assume f_j is a rotation-translation transformation, its inverse f_j^{-1} is also a rotation-translation transformation, which can be parameterized using a matrix $M_{f_j} \in \mathbb{R}^{2 \times 3}$ with the following form:

$$M_{f_j} = \begin{bmatrix} \cos \theta_j & -\sin \theta_j & b_j^1 \\ \sin \theta_j & \cos \theta_j & b_j^2 \end{bmatrix}, \quad (5)$$

where θ_j is the rotation angle, and $\mathbf{b}_j = (b_j^1, b_j^2)^T$ is the translation vector. Then, a pixel at location $(x_1, x_2)^T$ will be mapped to a new location $(x'_1, x'_2)^T$ after applying f_j^{-1} :

$$\begin{bmatrix} x'_1 \\ x'_2 \end{bmatrix} = M_{f_j} \cdot \begin{bmatrix} x_1 \\ x_2 \\ 1 \end{bmatrix} = \begin{bmatrix} x_1 \cos \theta_j - x_2 \sin \theta_j + b_j^1 \\ x_1 \sin \theta_j + x_2 \cos \theta_j + b_j^2 \end{bmatrix}. \quad (6)$$

Then we further parameterize $\{\theta_j, \mathbf{b}_j\}$ using a network block ϕ , referred to as transformation prediction block in Fig. 2, with Z_0, Z_j as its input:

$$\{\theta_j, \mathbf{b}_j\} = \phi(\text{concat}[Z_0, Z_j]), \quad (7)$$

such that we can directly predict the alignment transformation f_j^{-1} during inference.

3.2.3. Reconstruction Module

After alignment, the aligned features $\{\tilde{Z}_j\}_{j=0}^{B-1}$ of all frames (we let $\tilde{Z}_0 \triangleq Z_0$ for convenience) are then further processed for reconstructing the HR sRGB image.

Feature interaction. Before upsampling, interacting the features between the reference and source frames is important for enriching information of each frame. While existing methods either concatenate the features of reference and source frames directly [11, 12, 20] or use attention maps for pixel-wise interaction [33], there are still limitations in modeling capacity and computational efficiency. Therefore, we convert to another solution by adopting the MDTA block from Restormer [37]. The key designing mechanism behind MDTA is to apply self-attention across channels rather than spatial dimensions, computing cross-covariance to generate attention maps that implicitly encode global context. Such a design not only reduces computational complexity but also enables more effective feature integration by modeling long-range dependencies between features of the reference and source frames. The interaction process for the aligned features of all frames is as follows ($j = 0, \dots, B-1$):

$$\mathbf{Q}_j = W_d^Q W_p^Q (\text{concat}[\tilde{Z}_j, \tilde{Z}_0]), \quad (8)$$

$$\mathbf{K}_j = W_d^K W_p^K (\text{concat}[\tilde{Z}_j, \tilde{Z}_0]), \quad (9)$$

$$\mathbf{V}_j = W_d^V W_p^V (\text{concat}[\tilde{Z}_j, \tilde{Z}_0]), \quad (10)$$

$$\hat{Z}_j = \mathbf{V}_j \cdot \text{Softmax}(\mathbf{K}_j \cdot \mathbf{Q}_j / \alpha_j) + \tilde{Z}_j, \quad (11)$$

where $\{\hat{Z}_j\}_{j=0}^{B-1}$ are the features after interaction, $W_p^{(\cdot)}$ and $W_d^{(\cdot)}$ refer to 1×1 pixel-wise and 3×3 depth-wise convolutions, respectively, and α_j is a learnable scaling parameter. The term $\text{Softmax}(\mathbf{K}_j \cdot \mathbf{Q}_j / \alpha_j)$ captures feature correlations and dynamically weights value vectors based on similarity, enabling context-aware fusion. Compared with element-wise multiplication or concatenation, this attention mechanism is more effective in capturing global correlations and adjusting feature contributions. After the above interaction process, the features are expected to be sufficiently enriched and ready for upsampling and final fusion.

Upsampling and final fusion. For upsampling, we adopt the LTE framework [22], leveraging the INR technique and frequency domain processing, to recover the high-frequency details. LTE has two advantages particularly important for the BISR task. Firstly, as shown in [20], due to the nature of INR, the LTE-based architecture is good at multi-scale BISR, such that we can train a single model to cover multiple application scenarios. Secondly, as a core component of LTE, the grid sampling mechanism enables the upsampling of sub-pixel information from original frames. This is especially crucial for burst images since the fine-grained details introduced by slight camera shifts can be expected to be effectively recovered by such a mechanism. After upsampling, a fusion block with the channel

attention mechanism is introduced to fuse the upscaled features, and a skip connection is employed to also preserve the information from the original reference frame.

To be specific, the upsampling and final fusion process can be formulated as

$$I^S = \text{PS} \left(\tilde{I}_0^L \uparrow + \text{Avg}_W \left(\{\Phi_{\text{up}_j}(\hat{Z}_j)\}_{j=0}^{B-1} \right) \right), \quad (12)$$

where $I^S \in \mathbb{R}^{sh \times sw \times 3}$ is the final output in sRGB format, $\text{PS}(\cdot)$ denotes the pixel shuffle operation, $\text{Avg}_W(\cdot)$ refers to the weighted average operation with parameters learned via convolutions from \hat{Z}_j s, $\Phi_{\text{up}_j}(\cdot)$ denotes the LTE-based upsampling, and $\tilde{I}_0^L \uparrow \in \mathbb{R}^{(sh/2) \times (sw/2) \times 12}$ is the upsampled reference frame obtained by

$$\tilde{I}_0^L \uparrow = \text{Conv}_{1 \times 1}(\text{Up}[I_0^L]), \quad (13)$$

where $\text{Up}[\cdot]$ refers to the bilinear upsampling operation, and $\text{Conv}_{1 \times 1}(\cdot)$ is a 1×1 convolution layer.

3.2.4. Training loss

The whole network is trained in an end-to-end way using the following loss:

$$\mathcal{L} = \mathcal{L}_{\text{align}} + \mathcal{L}_{\text{fidelity}}, \quad (14)$$

where $\mathcal{L}_{\text{align}}$ is defined in Eq. (4), and $\mathcal{L}_{\text{fidelity}}$ is defined as

$$\mathcal{L}_{\text{fidelity}} = \|I^S - I^{\text{GT}}\|_1, \quad (15)$$

with I^{GT} being the ground truth HR sRGB image.

3.3. Theoretical justification

In this section, we provide theoretical results to show the validity of the proposed alignment framework. Due to space limitations, we only provide the sketch of the results, and the full presentations and proofs are provided in the supplementary material. Firstly, considering the discretization of the rotation angles in common Eq-CNN implementations, we have the following theorem.

Theorem 1 *For an image I_0 of size $H \times W \times C$, a rotation-translation Eq-CNN $g(\cdot)$ with discretized angles, and a rotation-translation transformation $f_j(\cdot)$, under certain assumptions, the following result holds:*

$$\|f_j^{-1}(g(f_j(I_0))) - g(I_0)\|_\infty \leq C_1 h^2 + C_2 p h t^{-1}, \quad (16)$$

where t, p, h, C_1, C_2 are constants.

Different from existing theories in Eq-CNN showing that input transformations can be predictably reflected in the feature domain, by measuring the error between $g(f_j(I_0))$ and $f_j(g(I_0))$, Theorem 1 further analyzes the residual errors caused by inverse transformation applied to these two objects in discrete settings of Eq-CNN, and suggests that such

an error can also be upper-bounded. Such an analysis provides a theoretical understanding of how input-level inverse transformations affect feature relationships, which advances the theory of Eq-CNN to a certain extent. With Theorem 1, we can easily obtain the following corollary.

Corollary 1 *Under the same assumptions and definitions of Theorem 1, for an image I_j with the same size of I_0 , let $Z_0 = g(I_0)$ and $Z_j = g(I_j)$ be the feature maps, where $Z_0, Z_j \in \mathbb{R}^{H \times W \times tC}$, and then the following result holds:*

$$\|f_j^{-1}(Z_j) - Z_0\|_\infty \leq C_3 \|f_j^{-1}(I_j) - I_0\|_2 + C_1 h^2 + C_2 p h t^{-1}, \quad (17)$$

where t, p, h, C_1, C_2, C_3 are constants.

Corollary 1 suggests that we can minimize the distance between $f_j^{-1}(Z_j)$ and Z_0 , the main goal in Section 3.2.2, through minimizing the distance between $f_j^{-1}(I_j)$ and I_0^L , which is we are trying to do by the loss defined in Eq. (4).

4. Experiments

In this section, we conduct experiments to validate the effectiveness of our proposed method. We first evaluate the proposed method on standard benchmarks for BSIR in comparison with existing methods. Then, we conduct ablation studies to demonstrate the reasonability of our method, specifically concerning the alignment mechanism.

4.1. Experiments on BSIR benchmarks

4.1.1. Settings

Datasets. We follow previous studies [12, 20] and conduct experiments on two datasets: **(1) SyntheticBurst Dataset [1]**, which consists of 46,839 burst sequences for training and 300 for validation. Each burst sequence contains 14 RAW LR frames generated from an HR sRGB image using the standard pipeline [11, 20]. Specifically, unprocessing techniques [5] are firstly applied to simulate RAW sensor data, and random rotations and translations are implemented to simulate real camera motion. Following [20], we generate multi-scale LR images through random downsampling ($\times 2$, $\times 3$, $\times 4$). Finally, Bayer mosaicking and random noise are added to more closely reproduce real-world imaging conditions. **(2) BurstSR Dataset [2]**, which comprises 200 full-size RAW burst sequences, with 5,405 patches of size 80×80 extracted for training and 882 patches for validation. The LR images are captured using a smartphone, while the HR ground truth images are obtained from a DSLR under the same scenes. Each LR burst sequence consists of 14 frames, and the scale factor between LR and HR images in this dataset is fixed ($\times 4$).

Competing methods and evaluation metrics. We evaluate our method against 8 representative ones, including

traditional Bicubic interpolation and current state-of-the-art methods for the BISR task: DBSR [2], MFIR [3], BIP-Net [11], GMTNet [25], Burstormer [12], BSRT [24], and BurstM [20]. We employ two widely used metrics, PSNR and SSIM, to quantitatively assess the reconstruction quality of each method. Additionally, we report model complexity metrics, including the number of parameters and GFLOPs, to show the computational efficiency of each method as a reference.

Implementation details. All experiments are implemented using PyTorch on an NVIDIA 4090 GPU. On the SyntheticBurst dataset, the initial learning rate for our model is set to 1×10^{-4} and gradually adjusted to 1×10^{-6} over 300 epochs. The batch size is 1, and the patch size is 48×48 . On the BurstSR dataset, we fine-tune the model pre-trained on SyntheticBurst following [12, 20], using an initial learning rate of 1×10^{-5} and CosineAnnealingLR to adjust it to 1×10^{-6} over 30 epochs. The batch size is 1, and the patch size is 80×80 . For other compared deep learning-based methods, we test using the author-released models, except GMTNet for which we directly quote the results reported in the original paper since the model is not released.

4.1.2. Results

Results on SyntheticBurst Dataset [1]. We present the quantitative and qualitative evaluation results in Table 1 and Fig. 3, respectively, with full-size and additional visual results available in the supplementary material because of space limitation.

As shown in Table 1, our method outperforms existing BISR approaches across nearly all evaluation metrics. Specifically, for the widely-used $\times 4$ SR setting, our method achieves the results with a PSNR of 43.18 and an SSIM of 0.974, surpassing competing methods with comparable model complexities. This quantitatively demonstrates its effectiveness in reconstructing the original HR sRGB image. Notably, our approach outperforms the current state-of-the-art multi-scale BISR method BurstM [20] while requiring fewer parameters and less FLOPs, showing both its efficiency and effectiveness. Furthermore, our method consistently performs well across different SR factor settings, suggesting its promising generalization ability. Visual results in Fig. 3 show that our method achieves competitive performance in several aspects. For example, our approach better preserves fine-grained textual details while maintaining structural fidelity. In addition, the method shows its ability to suppress noise without introducing unexpected artifacts or severe color distortions. These qualitative advantages of our method are consistent with its quantitative performance. It should be mentioned that though our model achieves slightly lower numeric results at the $\times 4$ scale due to its fewer parameters (8.7M) compared to BSRT-Large (20.71M), it delivers comparable visual quality. Additional visual results of other scales are provided in the supplement-

tary material for a more comprehensive comparison.

Results on BurstSR Dataset. The quantitative results on the BurstSR dataset are summarized in Table 1. It can be seen that our method achieves the best performance in terms of both PSNR and SSIM among all competing ones. Note that, in this real dataset, although the degradation process of the LR burst images is unknown, and the relationship between the source and reference frames might be more complex than assumed, our method still performs promisingly. This indicates that, though relatively simple, the rotation-translation assumption for the align transformation made in our model is rational and effective in real scenarios.

The visual results in Fig. 4 further validate the effectiveness of our approach. Overall, our method keeps more fine-grained details and produces fewer unexpected artifacts compared with existing methods. For example, as shown in the first row, our result better keeps the morphology of characters and digital numbers, and in the last row, our method can better suppress artifacts while producing relatively sharper edges. More visual results on this dataset are provided in the supplementary material.

4.2. Ablation Study

In this subsection, we conduct experiments on the SyntheticBurst dataset at $\times 4$ scale to validate the rationality and effectiveness of the proposed alignment framework in our model. The overall quantitative and visual results are summarized in Table 2 and shown in Fig. 5 - Fig. 6, respectively.

Effectiveness of the overall alignment module (a) & (b). We first replace the whole alignment module in our method with implicit alignment strategies using Restormer (a) and deformable convolutions (b).

As shown in Table 2, both methods exhibit significant performance degradation, which can be more intuitively observed in the visual results illustrated in Fig. 5 (a) and (b), that the fine-grained textures are not well kept. This can be attributed to the misalignment of features, as can be observed in Fig. 6 (a) and (b). These results clearly substantiate the effectiveness of our alignment module.

Effectiveness of equivariant feature extraction (c). We then conduct an ablation study by replacing the ENet, which is an Eq-CNN, with a V-CNN without the rotation equivariance for feature extraction. As shown in Table 2 (c) and Fig. 5 (c), this variant exhibits a noticeable performance drop compared to the proposed model in quantitative metrics and also produces blurry textures. The reason can be attributed to the lack of consistency of the alignment transformations between the image and feature domains, leading to mismatching among aligned features. This can be further substantiated by Fig. 7, within which we visualize the error maps of alignment results in both domains. It can be observed from this figure that, though the difference of image alignment is not very significant between the two variants,

Table 1. Quantitative results on SyntheticBurst and BurstSR datasets. The best and second-best results are highlighted in bold and underlined, respectively.

Method	SyntheticBurst						BurstSR		BurstSR	
	x2		x3		x4		x4		Params.(M)	FLOPs(G)
	PSNR	SSIM	PSNR	SSIM	PSNR	SSIM	PSNR	SSIM		
Bicubic	38.30	0.948	33.94	0.886	33.02	0.862	42.55	0.962	-	-
DBSR [2]	40.51	0.965	40.11	0.959	40.76	0.959	48.05	0.984	13.01	111.71
MFIR [3]	41.25	0.971	41.81	0.972	41.56	0.964	48.33	0.985	12.13	121.01
BIPNet [11]	37.58	0.928	40.83	0.955	41.93	0.960	48.49	0.985	6.7	326.47
Burstormer [12]	37.06	0.925	40.26	0.953	42.83	0.973	48.06	0.986	2.5	38.33
GMTNet [25]	-	-	-	-	42.36	0.961	48.95	0.986	-	300
BSRT-Small [24]	40.64	0.966	42.30	0.975	42.72	0.971	48.57	0.986	4.92	178.82
BSRT-Large [24]	40.33	0.965	42.87	0.979	43.62	0.975	48.57	0.986	20.71	362.63
BurstM [20]	46.01	0.985	44.79	0.982	42.87	0.973	49.12	0.987	14.0	436.21
Ours	46.10	0.985	44.95	0.983	<u>43.18</u>	<u>0.974</u>	49.22	0.987	8.7	170.21

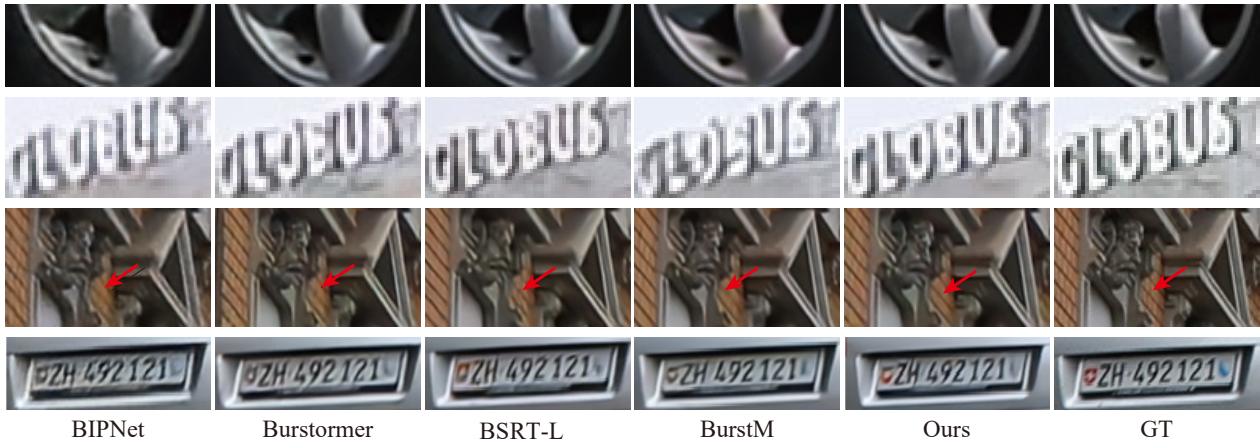


Figure 3. Visual comparison of x4 BISR on the SyntheticBurst dataset.

Table 2. Ablation Study with x4 SyntheticBurst Dataset

Settings	PSNR	SSIM	Params.(M)
(a) Align with RT	42.97	0.972	9.0
(b) Align with DConv	42.81	0.970	11.5
(c) w/o Eq-CNN	42.76	0.971	10.1
(d) w/o T-mat.	42.80	0.972	8.7
Ours	43.18	0.974	8.7

*RT: Restormer [37]

*DConv: Deformable convolution network [8]

*w/o Eq-CNN: Replacing Eq-CNN with conventional CNN

*w/o T-mat: Removing the transformation matrix

the Eq-CNN produces a much better alignment result than V-CNN in the feature domain. These results substantiate the reasonability and necessity of using Eq-CNN in our alignment framework.

Another interesting observation is that, though it does not perform well in the quantitative metrics, the visual results of this variant are comparable or even look better than that of other ablation variants as shown in Fig. 5, and the

alignment error in features is also significantly smaller than that of variants (a) and (b) as depicted in Fig. 6. This can be due to the explicit alignment mechanism using the learnable transformation and the translation-equivariance of V-CNNs, which indirectly suggests the effectiveness of our approach. **Effectiveness of the learnable transformation matrix (d).** We then remove the transformation matrix, denoted as “w/o T-mat.” in Table 2, and such a variant can be seen as implementing implicit alignment with the Eq-CNN. It can be observed from Fig. 6 (d) that this leads to obvious feature misalignment and correspondingly inferior performance both in quantitative metrics and visual quality, highlighting the crucial role of explicit alignment.

5. Conclusion and Discussion

In this work, we have proposed a new method for BISR. The key consideration of our method is the design of a new effective alignment framework for the BISR task with Eq-CNN. Within the proposed alignment framework, by the equivariance property of Eq-CNN, the align transforma-

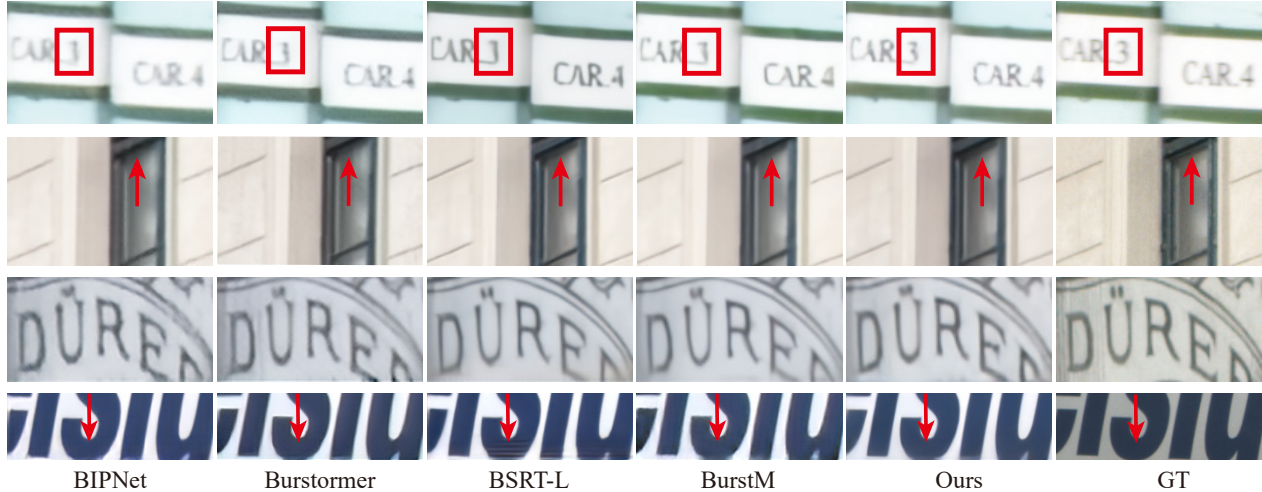


Figure 4. Visual comparison of $\times 4$ BISR on the BurstSR dataset.

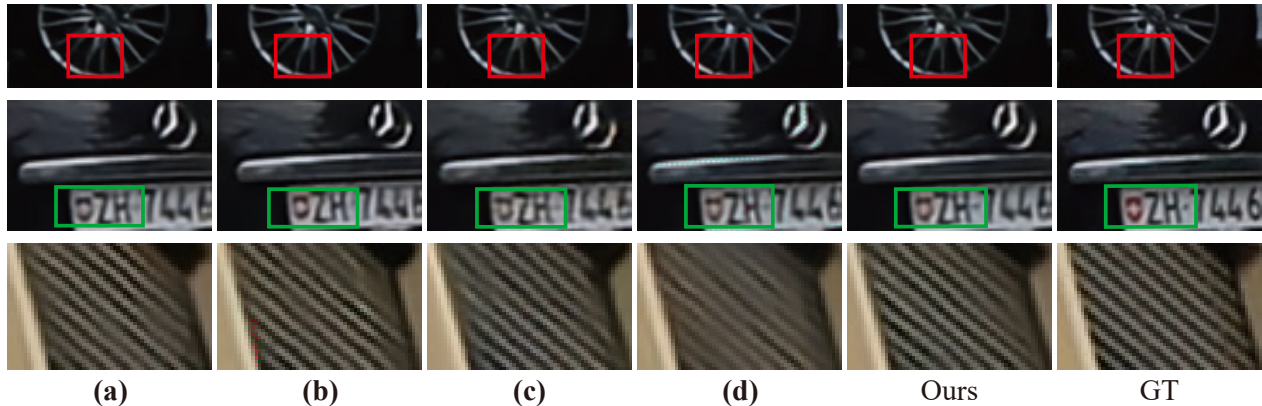


Figure 5. Visual results of the ablation study for $\times 4$ BISR on SyntheticBurst. The settings of (a)-(d) are referred to Table 2 and Section 4.2.

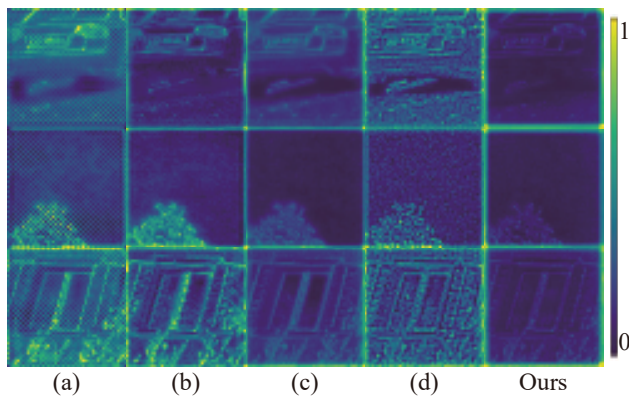


Figure 6. Error maps of aligned features for ablation studies on $\times 4$ burst super-resolution using the SyntheticBurst dataset. Detailed settings of (a)-(d) can be referred to Table 2 and Section 4.2.

tion can be learned with explicit image domain supervision and directly applied in the feature domain in a theoretically sound way. In addition, we have introduced effective up-sampling and fusion blocks using advanced neural architectures, including MDTA from Restormer and INR. Extensive experiments on two representative BISR benchmarks have been conducted, showing the effectiveness of the pro-

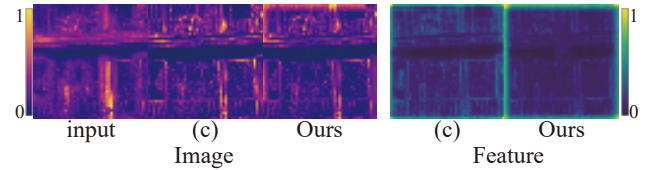


Figure 7. Visual comparison of alignment error maps between CNN (c) Eq-CNN (Ours) in the image (left) and feature (right) domains, evaluated on the $\times 4$ BISR task using the SyntheticBurst dataset. The error map is defined by measuring the pixel-wise difference between the reference and source frames. proposed method, both quantitatively and visually, against current state-of-the-art methods.

Despite its promising performance for BISR, our method still has limitations that need further investigation. For example, currently, the transformation considered in our model is restricted to rotation and translation due to the ability of existing Eq-CNNs, which may not be precise enough to characterize the relationship between the reference and source frame in complex real-world scenarios. Tackling this issue requires developing new techniques and theories for equivariance networks, which could not only enhance the availability of our method in real applications but also advance the study of equivariance in deep learning.

References

- [1] Goutam Bhat, Martin Danelljan, and Radu Timofte. Ntire 2021 challenge on burst super-resolution: Methods and results. In *Proceedings of the IEEE/CVF Conference on Computer Vision and Pattern Recognition*, pages 613–626, 2021. 1, 2, 3, 5, 6
- [2] Goutam Bhat, Martin Danelljan, Luc Van Gool, and Radu Timofte. Deep burst super-resolution. In *Proceedings of the IEEE/CVF conference on computer vision and pattern recognition*, pages 9209–9218, 2021. 2, 5, 6, 7
- [3] Goutam Bhat, Martin Danelljan, Fisher Yu, Luc Van Gool, and Radu Timofte. Deep reparametrization of multi-frame super-resolution and denoising. In *Proceedings of the IEEE/CVF international conference on computer vision*, pages 2460–2470, 2021. 2, 6, 7
- [4] Goutam Bhat, Martin Danelljan, Radu Timofte, Yizhen Cao, Yuntian Cao, Meiya Chen, Xihao Chen, Shen Cheng, Akshay Dudhane, Haoqiang Fan, et al. Ntire 2022 burst super-resolution challenge. In *Proceedings of the IEEE/CVF conference on computer vision and pattern recognition*, pages 1041–1061, 2022. 1
- [5] Tim Brooks, Ben Mildenhall, Tianfan Xue, Jiawen Chen, Dillon Sharlet, and Jonathan T Barron. Unprocessing images for learned raw denoising. In *Proceedings of the IEEE/CVF conference on computer vision and pattern recognition*, pages 11036–11045, 2019. 5
- [6] Yinbo Chen, Sifei Liu, and Xiaolong Wang. Learning continuous image representation with local implicit image function. In *Proceedings of the IEEE/CVF conference on computer vision and pattern recognition*, pages 8628–8638, 2021. 2
- [7] Taco Cohen and Max Welling. Group equivariant convolutional networks. In *International conference on machine learning*, pages 2990–2999. PMLR, 2016. 2
- [8] Jifeng Dai, Haozhi Qi, Yuwen Xiong, Yi Li, Guodong Zhang, Han Hu, and Yichen Wei. Deformable convolutional networks. In *Proceedings of the IEEE international conference on computer vision*, pages 764–773, 2017. 2, 7
- [9] Xin Di, Long Peng, Peizhe Xia, Wenbo Li, Renjing Pei, Yang Cao, Yang Wang, and Zheng-Jun Zha. Qmambabsr: Burst image super-resolution with query state space model. *arXiv preprint arXiv:2408.08665*, 2024. 2
- [10] Chao Dong, Chen Change Loy, Kaiming He, and Xiaoou Tang. Image super-resolution using deep convolutional networks. *IEEE transactions on pattern analysis and machine intelligence*, 38(2):295–307, 2015. 1
- [11] Akshay Dudhane, Syed Waqas Zamir, Salman Khan, Fahad Shahbaz Khan, and Ming-Hsuan Yang. Burst image restoration and enhancement. In *Proceedings of the IEEE/CVF Conference on Computer Vision and Pattern Recognition*, pages 5759–5768, 2022. 2, 4, 5, 6, 7
- [12] Akshay Dudhane, Syed Waqas Zamir, Salman Khan, Fahad Shahbaz Khan, and Ming-Hsuan Yang. Burstformer: Burst image restoration and enhancement transformer. In *2023 IEEE/CVF Conference on Computer Vision and Pattern Recognition (CVPR)*, pages 5703–5712. IEEE, 2023. 2, 3, 4, 5, 6, 7
- [13] M. Elad and A. Feuer. Restoration of a single super-resolution image from several blurred, noisy, and undersampled measured images. *IEEE Transactions on Image Processing*, 6(12):1646–1658, 1997. 2
- [14] Jiahong Fu, Qi Xie, Deyu Meng, and Zongben Xu. Rotation equivariant proximal operator for deep unfolding methods in image restoration. *IEEE Transactions on Pattern Analysis and Machine Intelligence*, 2024. 2, 3
- [15] Albert Gu and Tri Dao. Mamba: Linear-time sequence modeling with selective state spaces. *arXiv preprint arXiv:2312.00752*, 2023. 2
- [16] Jonathan Ho, Ajay Jain, and Pieter Abbeel. Denoising diffusion probabilistic models. *Advances in neural information processing systems*, 33:6840–6851, 2020. 2
- [17] Emiel Hoogeboom, Jorn WT Peters, Taco S Cohen, and Max Welling. Hexaconv. *arXiv preprint arXiv:1803.02108*, 2018. 2
- [18] Berthold KP Horn and Brian G Schunck. Determining optical flow. *Artificial intelligence*, 17(1-3):185–203, 1981. 2
- [19] Michal Irani and Shmuel Peleg. Improving resolution by image registration. *CVGIP: Graphical models and image processing*, 53(3):231–239, 1991. 2
- [20] EungGu Kang, Byeonghun Lee, Sunghoon Im, and Kyong Hwan Jin. Burstm: Deep burst multi-scale sr using fourier space with optical flow. In *European Conference on Computer Vision*, pages 459–477. Springer, 2025. 2, 3, 4, 5, 6, 7
- [21] Alex Krizhevsky, Ilya Sutskever, and Geoffrey E Hinton. Imagenet classification with deep convolutional neural networks. *Advances in neural information processing systems*, 25, 2012. 2
- [22] Jaewon Lee and Kyong Hwan Jin. Local texture estimator for implicit representation function. In *Proceedings of the IEEE/CVF conference on computer vision and pattern recognition*, pages 1929–1938, 2022. 2, 4
- [23] Bee Lim, Sanghyun Son, Heewon Kim, Seungjun Nah, and Kyoung Mu Lee. Enhanced deep residual networks for single image super-resolution. In *Proceedings of the IEEE conference on computer vision and pattern recognition workshops*, pages 136–144, 2017. 2
- [24] Ziwei Luo, Youwei Li, Shen Cheng, Lei Yu, Qi Wu, Zhihong Wen, Haoqiang Fan, Jian Sun, and Shuaicheng Liu. Bsrt: Improving burst super-resolution with swin transformer and flow-guided deformable alignment. In *Proceedings of the IEEE/CVF Conference on Computer Vision and Pattern Recognition*, pages 998–1008, 2022. 2, 6, 7
- [25] Nancy Mehta, Akshay Dudhane, Subrahmanyam Murala, Syed Waqas Zamir, Salman Khan, and Fahad Shahbaz Khan. Gated multi-resolution transfer network for burst restoration and enhancement. In *2023 IEEE/CVF Conference on Computer Vision and Pattern Recognition (CVPR)*, pages 22201–22210. IEEE, 2023. 2, 6, 7
- [26] Andrea Bordone Molini, Diego Valsesia, Giulia Fracastoro, and Enrico Magli. Deepsum: Deep neural network for super-resolution of unregistered multitemporal images. *IEEE Transactions on Geoscience and Remote Sensing*, 58(5):3644–3656, 2019. 2

- [27] Kyotaro Tokoro, Kazutoshi Akita, and Norimichi Ukita. Burst super-resolution with diffusion models for improving perceptual quality. *arXiv preprint arXiv:2403.19428*, 2024. [2](#)
- [28] Roger Y Tsai and Thomas S Huang. Multiframe image restoration and registration. *Multiframe image restoration and registration*, 1:317–339, 1984. [2](#)
- [29] Hanoch Ur and Daniel Gross. Improved resolution from sub-pixel shifted pictures. *CVGIP: Graphical models and image processing*, 54(2):181–186, 1992. [2](#)
- [30] Evgeniya Ustinova and Victor Lempitsky. Deep multi-frame face super-resolution. *arXiv preprint arXiv:1709.03196*, 2017. [2](#)
- [31] A Vaswani. Attention is all you need. *Advances in Neural Information Processing Systems*, 2017. [2](#)
- [32] Zhihao Wang, Jian Chen, and Steven CH Hoi. Deep learning for image super-resolution: A survey. *IEEE transactions on pattern analysis and machine intelligence*, 43(10):3365–3387, 2020. [1](#)
- [33] Pengxu Wei, Yujing Sun, Xingbei Guo, Chang Liu, Guanbin Li, Jie Chen, Xiangyang Ji, and Liang Lin. Towards real-world burst image super-resolution: Benchmark and method. In *Proceedings of the IEEE/CVF International Conference on Computer Vision*, pages 13233–13242, 2023. [4](#)
- [34] Maurice Weiler, Fred A Hamprecht, and Martin Storath. Learning steerable filters for rotation equivariant cnns. In *Proceedings of the IEEE Conference on Computer Vision and Pattern Recognition*, pages 849–858, 2018. [2](#), [3](#)
- [35] Qi Xie, Qian Zhao, Zongben Xu, and Deyu Meng. Fourier series expansion based filter parametrization for equivariant convolutions. *IEEE Transactions on Pattern Analysis and Machine Intelligence*, 45(4):4537–4551, 2022. [3](#)
- [36] Qi Xie, Qian Zhao, Zongben Xu, and Deyu Meng. Fourier series expansion based filter parametrization for equivariant convolutions. *IEEE Transactions on Pattern Analysis and Machine Intelligence*, 45(4):4537–4551, 2022. [2](#)
- [37] Syed Waqas Zamir, Aditya Arora, Salman Khan, Munawar Hayat, Fahad Shahbaz Khan, and Ming-Hsuan Yang. Restormer: Efficient transformer for high-resolution image restoration. In *Proceedings of the IEEE/CVF conference on computer vision and pattern recognition*, pages 5728–5739, 2022. [2](#), [4](#), [7](#)